Applied Catalysis B: Environmental 156–157 (2014) 378–384

Contents lists available at ScienceDirect

Applied Catalysis B: Environmental

journal homepage: www.elsevier.com/locate/apcatb

Platinum loaded $NaNbO_{3-x}N_x$ with nanostep surface nanostructures toward enhanced visible-light photocatalytic activity

Haifeng Shi[a,b,*], Guoqing Chen[a], Zhigang Zou[b]

[a] School of Science, Jiangnan University, Wuxi 214122, PR China
[b] Eco-materials and Renewable Energy Research Center (ERERC), Department of Physics, Nanjing University, Nanjing 210093, PR China

ARTICLE INFO

Article history:
Received 16 December 2013
Received in revised form 12 March 2014
Accepted 19 March 2014
Available online 28 March 2014

Keywords:
$NaNbO_3$
Photocatalytic
Nitrogen doping
Pt loading
Surface nanostructure

ABSTRACT

Pt loaded $NaNbO_{3-x}N_x$ (Pt-NNON), a visible-light-sensitive photocatalyst, was synthesized by an in situ photodeposition method from $H_2PtCl_6{\cdot}6H_2O$ onto $NaNbO_{3-x}N_x$ (NNON) sample. Pt-NNON exhibited a much higher photocatalytic activity for gaseous 2-propanol (IPA) degradation under visible-light irradiation in contrast to NNON. The apparent quantum efficiency (AQE) of Pt-NNON sample for IPA photodegradation achieved up to 8.6% at the wavelength of 419 nm. The notably enhanced photocatalytic performance was attributed to the promoted charge separation and transfer capability in the Pt-NNON system. This work suggests that surface nanosteps possibly play an important role as an electron transfer at high way, which facilitates to the charge carrier collection onto Pt rich zones and thus suppresses recombination between photogenerated electrons and holes. This method can thus be considered as an excellent strategy to enhance photocatalytic activity of organic decomposition in addition to the commonly applied noble metal doping method.

1. Introduction

The increasing and urgent request for environmental remediation and solar energy conversion is becoming more and more important in the view of humans' continuable development. The photocatalysis technique using semiconductors and sunlight has been consistently gaining attention as one of the potential and promising avenues to solve environmental issues facing mankind during the past four decades [1–11]. Especially, as a green chemistry technology, photocatalysis can decompose organic pollutants ultimately into harmless chemicals such as CO_2, H_2O, and mineral acids (without the secondary waste products) [12]. Moreover, the photocatalytic reaction occurs at room temperature and ambient pressure, which is a benign approach that is undoubtedly superior to the traditional combustion treatment technique. Up to now, among the present photocatalysts for decomposing organic compounds, TiO_2-based semiconductor photocatalysts have been the most popular due to its high activity, wide availability, and strong photostability. One of the major disadvantages of TiO_2, however, is that the relative wide band gaps (anatase: 3.2 eV; rutile: 3.0 eV) undoubtedly limit their photocatalytic performance only sensitive in the ultraviolet light (UV) region (~4% of solar spectrum reaching the Earth). In contrast to the UV range, the visible region of the solar spectrum accounts for ~43% of the sunlight incident on the surface of the Earth. In order to effectively utilize solar energy or indoor lighting, it is appealing to develop visible-light-sensitive photocatalysts that are efficient enough for use in daily life for environmental cleaning. Recently, various modified TiO_2 (cation- or anion- doped TiO_2) [13–16] and some multiple-metal oxide materials [17–22] have been reported as photocatalysts with improved efficiency toward degradation of organic compounds under visible-light illumination. However, the efficiencies of photocatalysts harvesting visible light to decompose organic compounds are still limited due to the high recombination rates of photogenerated electron–hole pairs.

Generally, the photocatalytic organic compounds decomposition reaction involves three steps: (1) the generation of electrons/holes under irradiation of light matched with the energy band gap of a photocatalyst, (2) the photoexcited electrons/holes transfer to the semiconductor surface and further react with the surrounding organic species, and (3) the recombination of the separated photoexcited electron/hole pairs is likely to occur in the volume or on the surface of the semiconductor particle, which will directly restrict the photocatalytic activity [2]. Thus, the efficient charge separation and suppression of recombination between photogenerated electrons and holes are very important for efficient photocatalytic degradation of organic compounds. As

* Corresponding author at: School of Science, Jiangnan University, Wuxi 214122, PR China. Tel.: +86 51085190601.
E-mail address: shihaifengnju@hotmail.com (H. Shi).

http://dx.doi.org/10.1016/j.apcatb.2014.03.036
0926-3373/

a consequence, one of the important principles of photocatalytic performance enhancement is to increase the separation efficiency of electron and hole pairs. Actually, loading noble metals (cocatalysts) on a photocatalyst has been proved as an effectual approach to improve their photocatalytic activities owing to the formation of a schottky barrier at the metal/semiconductor interface. Due to different work functions of noble metals and semiconductors, the photoinduced electrons preferentially migrate from the conduction band of the semiconductors to the noble metals, leading to the improved charge separation and reduced charge recombination [23–26].

Except for the appropriate noble metals loading, control of the surface morphology is one of important issues for improving the photocatalytic performance since the photocatalytic reactions precede on the surfaces [1]. For example, the surface nanostep structure over La-doped $NaTaO_3$ sample was constructed and observed to enhance the photocatalytic water splitting activity owing to the nanosteps structures with the advantage toward improved separation of electron–hole pairs [27]. Considering the benefits of nanostep structures, several photocatalysts with nanostep surface structures, such as $(AgIn)_xZn_{2(1-x)}S_2$[28], CdS[29], Sr-$NaTaO_3$[30], metal ions (Ca, Sr, and Ba)-doped $NaTaO_3$[31], $AgNbO_3$[32] were developed as photocatalysts for photocatalytic water splitting. However, to the best of our knowledge, there are few reports about the photocatalysts with nanostep structures for photodegradation of organic compounds.

Now the question is whether the combined such two strategies could be employed to effectively enhance the photocatalytic activity for organic decomposition? The present work has given a clear and positive answer. Herein, in this study, Pt loaded nitrogen doped $NaNbO_3$ (Pt-NNON) with nanostep surface microstructure was successfully synthesized and employed for gaseous IPA photodegradation. The physical characteristics of samples were examined by the techniques, such as XRD, UV–vis diffuse reflectance spectroscopy, FE-SEM, XPS, and BET measurement. In contrast to NNON, commercial N-TiO_2 (TPS201; Sumitomo Corp., Japan), and Pt-N-TiO_2, Pt-NNON exhibited a much higher activity of photocatalytic IPA degradation under visible-light irradiation. The possible mechanism of the activity enhancement over Pt-NNON was discussed in view of the charge carriers efficient separation and transport.

2. Experimental

2.1. Catalyst synthesis

Nitrogen-doped $NaNbO_3$ ($NaNbO_{3-x}N_x$, NNON) was prepared by nitriding the $NaNbO_3$ (NNO) precursor according to a previous report [33]. All chemical reagents were of analytical grade and used as received without further purification. In a typical procedure, the stoichiometric amounts of Na_2CO_3 (Junsei Co., Japan) and Nb_2O_5 (Wako Co., Japan) were well ground with ethanol and pretreated at 1073 K for 4 h, and then were reground and calcined at the temperature of 1173 K for 5 h. The so-obtained NNO powders were annealed at 833 K for 3 h under gaseous ammonia flow (flow rate: 40 ml/min). After nitrogen doping, the powders were cooled to room temperature under N_2 flow to remove the adsorbed ammonia molecules on the sample surface. The Pt-NNON sample was synthesized by an in situ photodeposition method. In a typical case, 0.5 g NNON photocatalyst, 320 mL distilled water, 50 mL CH_3OH, and a given amount (0.5%) of $H_2PtCl_6{\cdot}6H_2O$ were placed in an inner irradiation type Pyrex cell, followed by irradiation from a 400 W high-pressure Hg lamp with continuously stirring. After 4 h of irradiation, the suspension was filtered and dried for 12 h. For comparison, the Pt-N-TiO_2 was prepared following the similar procedure as mentioned above.

2.2. Sample characterization

The crystal structures of samples were measured by an X-ray diffractometer (Utilma III., Japan) in the 2θ range of 20–80°. The diffuse reflectance spectra of the samples were measured in the range of 250–700 nm by a UV–vis spectrophotometer (UV-2550; Shimadzu, Japan) equipped with an integrating sphere attachment and transformed to the absorption spectra according to the Kubelka–Munk relation, $K/S = (1-R)^2/2R$, where R is the value of reflectance measurements (the relative value to the reference of $BaSO_4$), K and S means the absorption and scattering coefficients of the sample, respectively. Morphologies of samples were characterized by a field-emission scanning electron microscope (FE-SEM; FEI Tecnai G2 F30, USA). The specific surface areas were deduced according to Brunauer–Emmett–Teller method using a nitrogen adsorption apparatus (TriStar-3000, Micrometrics, USA) at 77 K. X-ray photoelectron spectroscopy (XPS) analysis was measured on a PHI 5000 versaprobe instrument (ULVAC-PHI, Chigasaki, Japan) using Al Ka monochromatic X-ray radiation. The peak positions were corrected against the C1 speak (285.0 eV) of contaminated carbon.

2.3. Evaluation of photocatalytic activity

In this study, 2-propanol (C_3H_8O, *iso*-propanol, IPA) was used as the model organic pollutant to evaluate the photocatalytic performance. The catalyst (ca. 0.4 g) was uniformly and evenly dispersed on the bottom of a small glass cell (area = 8.0 cm^2) that was located in a 0.5 L cylindrical quartz reactor. After sealing the sample in the vessel and injecting the desired volume of gaseous IPA into the vessel using a syringe, the reactor was stored in the dark condition until an adsorption–desorption equilibrium was reached. Finally, the reactor was irradiated with the visible light, which was irradiated from a 300-W Xe lamp through a glass filter (Y44, Hoya Co., Japan) and a filter with circulating cooling water (removing the infrared ray light irradiation in order to avoid thermal catalytic effects). The gaseous products periodically extracted from the reaction cell to analyze the gas concentration with a gas chromatograph system (GC-9790A, Fuli, China) using a flame ionization detector (FID) for organic compounds determination. Commercial nitrogen doped TiO_2 (Com-N-TiO_2, TPS201; Sumitomo Corp., Japan) and Pt-N-TiO_2 were employed as reference photocatalysts to compare the photocatalytic activity under the same experimental conditions.

2.4. Calculation models and methods

The *ab initio* calculations described here were performed by a CASTEP program package based on the density functional theory [34]. Ultrasoft pseudopotentials were selected to describe the interactions between ionic cores and valence electrons. Generalized gradient approximations (GGA-PBE) were used to describe the exchange-correlation potentials. A plane wave basis set was employed to describe the electronic wave functions with a kinetic energy cutoff of 370 eV. The Brillouin-zone (BZ) integrations of total energy were calculated by the special $3 \times 3 \times 1$ k point in the Monkhorst–Pack scheme. Before single point energy calculations, geometry optimization was carried out by minimizing the total energy and atomic force. In $NaNbO_{3-x}N_x$ (NNON) unit model supercell, x value was 0.03125.

3. Results and discussion

3.1. Characterization of photocatalysts

Fig. 1 shows the XRD patterns of NNO, NNON, Pt-NNON samples. The diffraction peaks of NNO sample could be indexed to an

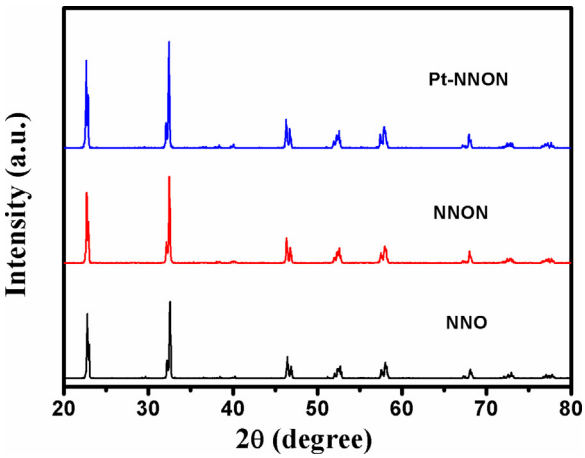

Fig. 1. X-ray diffraction patterns of Pt-NNON, NNON, and NNO samples.

orthorhombic-structured $NaNbO_3$, in good agreement with those in the JCPDS Card (No. 01-072-7753). The NNON maintained the crystal structure of NNO and no notably peak shift was detected by XRD measurement. This is reasonable since the nitrogen doping concentration (Pt-$NaNbO_{3-x}N_x$, $x \sim 0.03$) is too low to bring a notable XRD peak shift, although the ionic radius of N^{3-} (1.71 Å) is larger than that of O^{2-} (1.40 Å) [35]. In addition, the loading of Pt in the synthesis process basically did not affect the XRD patterns since the Pt loading content was only ~0.5%.

The optical absorption property of a photocatalyst is recognized as one of the important factors in determining its activity. Fig. 2a shows the UV–vis diffuse reflectance spectra of Pt-NNON, NNON, and NNO samples. The absorption threshold of NNO was approximately at 365 nm. While the absorption spectrum of NNON showed an enhanced light absorption up to 480 nm, which was ascribed by the newly formed N 2p band that was located slightly above the valence band consisting of O 2p states [33]. In addition, the absorption spectrum of Pt-NNON sample exhibited an improved light absorption in contrast to NNON in the visible-light region at $\lambda > 400$ nm, which was assigned to the interband and intraband transitions of Pt nanoparticles [36]. The inset of Fig. 2a displays the pictures of NNO, NNON, and Pt-NNON powders. It could be seen that the color of NNON changed from white to yellow after nitriding, while the Pt loading Pt-NNON sample turned to be grey, which was consistent with the absorption spectra (Fig. 2a). This clearly demonstrated that the spectral response of the NNO could be tuned to red shift effectively by nitrogen doping and Pt loading so as to have potential applications in the visible-light region.

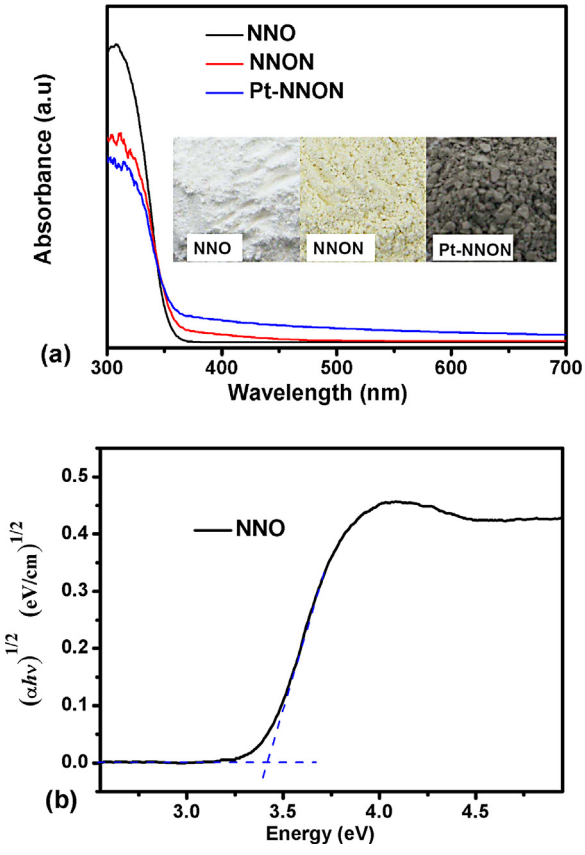

Fig. 2. (a) UV-vis diffuse reflectance spectra of Pt-NNON, NNON, and NNO samples, the inset displays the pictures of NNO, NNON, and Pt-NNON powders, and (b) a plot of $(\alpha h\nu)^{1/2}$ versus energy for NNO sample.

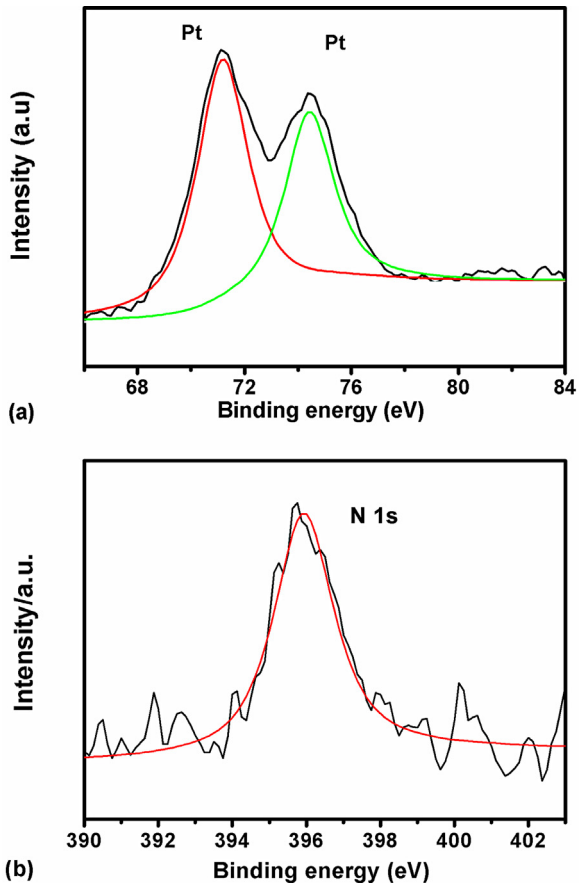

Fig. 3. XPS spectra of Pt-NNON. High-resolution XPS spectrum of: (a) Pt and (b) N.

The optical band gap E_g of a semiconductor could be deduced according to the following equation $(\alpha h\nu)^n = A(h\nu - E_g)$, where α means the absorption coefficient, $h\nu$ is the incident photo energy, the value of the index n depends on the electronic transition of the semiconductor ($n_{direct} = 2$; $n_{indirect} = 1/2$), A is a proportionality constant related to the material, and E_g means the band gap energy of the semiconductor, respectively. The band gap energy was obtained from the intercept of the tangent line in the plot of $(\alpha h\nu)^{1/2}$ versus energy, and the value was determined to be ~3.4 eV for NNO (Fig. 2b). The surface composition and state of the Pt-NNON was further investigated using X-ray photoelectron spectroscopy (XPS). As shown in the wide-scan XPS spectrum (Figure S1), no obvious impurity peak can be detected. The two peaks (Fig. 3a) located at 71.0 eV and 74.4 eV could be attributed to Pt $4f_{5/2}$ and Pt $4f_{7/2}$ [37,38], signifying the presence of Pt^0 metal

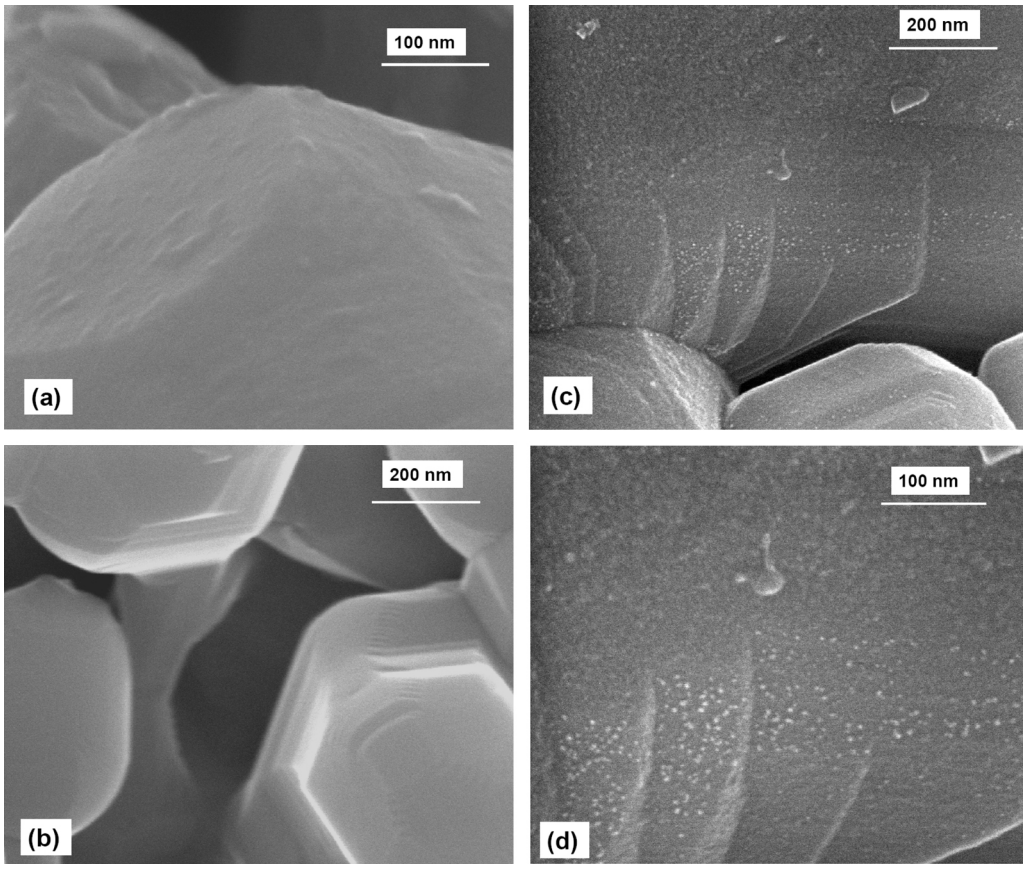

Fig. 4. FE-SEM images of (a) NNO, (b) NNON, (c) and (d) Pt-NNON samples.

loading on the Pt-NNON surface. Fig. 3b shows the XPS spectra for the N 1s of Pt-NNON. It can be seen that N 1s peak position was evaluated to be ~395.8 eV, which is similar to the results reported for N-$Sr_2Nb_2O_7$ [39], indicating that the nitrogen atoms have been successfully doped into NNO. In addition, the nitrogen concentration in Pt-NNON was estimated to be ~0.03 from XPS spectra.

The morphologies of Pt-NNON, NNON, and NNO samples were investigated by field emission scanning electron microscopy (FE-SEM). As shown in Fig. 4(a) and (b), the surface nanostep structures were observed for NNNO whereas the surfaces of NNO were relatively flat. These nanosteps were possible self-constructed during the heat treatment process of NNON likewise in the case of creation of the nanostep structures in La-$NaTaO_3$ [27]. As shown in Fig. 4(c) and (d), the Pt nanoparticles were mainly loaded on the nanostep areas of the particle's surface with an ultrafine size, which was similar in the case of Pt loaded $(AgIn)_xZn_{2(1-x)}S_2$ [28]. The more pictures of FE-SEM and EDS of Pt-NNON could be seen in Figure S2. This indicated that Pt nanoparticles tended to be mainly deposited at a certain position, that is, the considerable enrichment of Pt loaded at the nanostep area compared to the other areas. Therefore, it can be inferred that the photodeposited Pt nanoparticles might exist in the form of ultrafine particles and these Pt nanoparticles preferably exist at the nanostep areas.

3.2. Photocatalytic activities of photocatalysts

Gaseous IPA is usually taken as a model organic compound for evaluating the activity of a semiconductor photocatalyst. IPA photodegradation usually proceeds via an intermediate (acetone) route, namely, IPA is firstly photodegradated to acetone and eventually photo-oxidized to CO_2. Hence the photocatalytic activity is generally evaluated by the evolved acetone concentration at the initial stage [40–42]. Fig. 5 represents acetone evolution concentrations over Pt-NNON and NNON samples under visible-light irradiation. It was observed that the acetone generated and increased with the prolongation of irradiation time over all the catalysts. As shown in Fig. 5, the acetone generation rate of Pt-NNON was higher than that of NNON, indicating that the Pt-NNON catalyst has fairly good activity under visible-light irradiation. In addition, there was hardly any acetone to be observed either under dark conditions or without any catalyst. This implied that the reaction strongly depended on light and catalyst. Namely, the reaction was indeed a photocatalytic oxidization process. It was worthwhile to

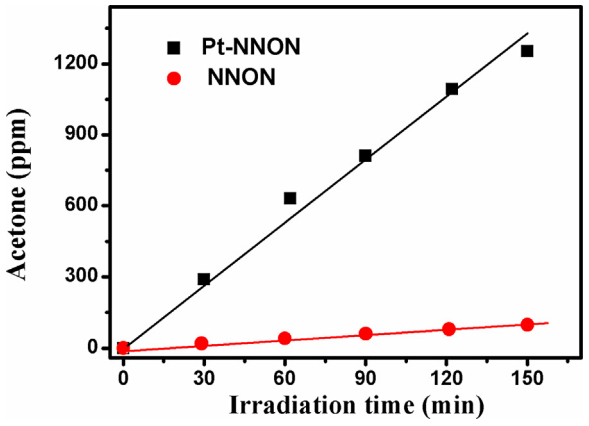

Fig. 5. Photocatalytic evolved acetone concentrations over Pt-NNON and NNON samples under-visible-light irradiation. Reaction conditions: light source, a 300 W Xe lamp with Y44 filter and water filter; Catalyst, 400 mg; the initial concentration of IPA is ~3300 ppm.

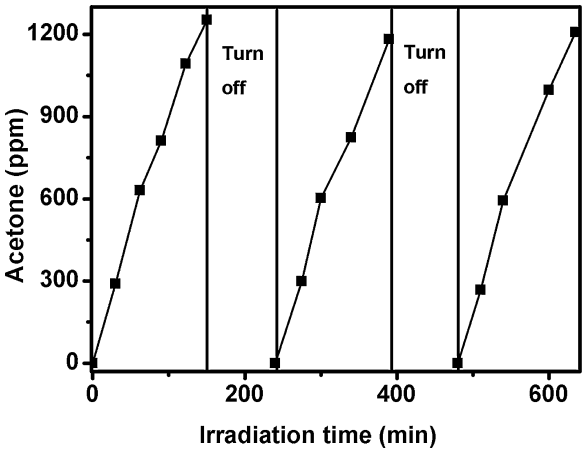

Fig. 6. Photocatalytic acetone evolution concentrations over Pt-NNON sample under visible-light irradiation. The initial concentration of IPA is ~3300 ppm.

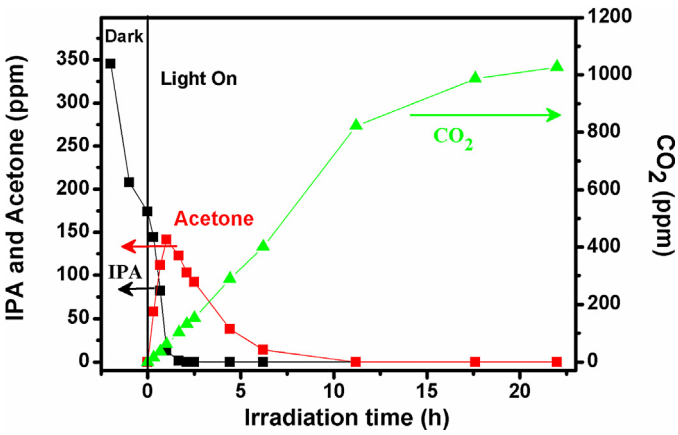

Fig. 7. Variations in gas concentrations over Pt-NNON sample under visible-light irradiation. The initial concentration of IPA is ~345 ppm.

note that the conversion rate of photo-oxidation of IPA into acetone reached 39% after a 150 min photocatalytic degradation reaction when the initial concentration as high as ~3300 ppm, indicating Pt-NNON was possibly a promising visible-light-sensitive photocatalyst. In order to investigate the photocatalytic repeatability of the catalyst, the photocatalytic oxidation of IPA over used Pt-NNON sample was performed again. It was revealed that the photocatalytic activity of used sample was similar to that of the fresh sample (Fig. 6). It is generally acknowledged that the IPA photo-oxidization proceeds two types of reaction processes as follows [43,44]:

(i) One-photon reaction process:

$$CH_3CHOHCH_3 + e^- + O_2 + H^+ \rightarrow CH_3COCH_3 + HO^\bullet + H_2O$$

Or

$$CH_3CHOHCH_3 + h^+ \rightarrow CH_3COCH_3 + 2H^+ + e^-;$$

(ii) Multi-photon reaction process:

$$CH_3CHOHCH_3 + 5H_2O + 18h^+ \rightarrow 3CO_2 + 18H^+.$$

Hence the apparent quantum efficiency (AQE) was calculated using the following equation: $AQE = N_{rp}/N_{ip} = (N_{ace} + 6N_{CO_2})/N_{ip}$ [17], where N_{rp} means the number of photons involved in the reaction of acetone generation, N_{ace} is the number of evolved acetone molecules, N_{ace} the number of generated CO_2 molecules, and N_{ip} means the number of incident photons. Using an interference filter ($\lambda = 419.1$ nm, $T_{max} = 40.4\%$), the apparent quantum efficiency (AQE) of Pt-NNON at $\lambda = 419.1$ nm was measured to be ~8.6%, indicating the Pt-NNON sample was active under visible-light irradiation.

To further evaluate the photocatalytic activity of Pt-NNON, the photocatalytic mineralization of gaseous IPA was conducted. As shown in Fig. 7, the initial concentration of IPA is ~345 ppm, while 171 ppmv of IPA was adsorbed on Pt-NNON and no acetone was detected after 2 h of dark adsorption. Upon visible-light irradiation, acetone in the gas phase was detected; while the observed concentration of acetone increased and reached the maximum level after ~1 h of light irradiation; meanwhile, IPA concentration decreased drastically and reached zero after ~100 min. It was noted that the rate of acetone generation was higher than that of CO_2 at the initial stage, implying that the photocatalytic decomposition of IPA into acetone is easier than the mineralization of acetone into CO_2. This is understandable since the evolution of each acetone molecule from IPA usually requires one hole, while the conversion of acetone into CO_2 is a more complex multi-hole-involved process [41,42]. The final concentration of CO_2 (~1027 ppm) over Pt-NNON after 22 h of reaction was nearly three times as many as the initially injected IPA (~345 ppm). Namely, almost all the injected IPA was mineralized into CO_2 and eventually achieved the carbon balance. Fig. 8 displays a comparison of the XRD patterns of Pt-NNON before and after the photocatalytic reaction. It could be seen that there was no obvious peak change in the XRD patterns of Pt-NNON before and after the photocatalytic reaction, indicating that the phase of Pt-NNON catalyst was a stable photocatalyst without occurrence of structural degradation during the present photocatalytic reaction process.

3.3. Mechanism of enhanced photocatalytic activity

Fig. 9 shows the BET surface areas and the acetone evolution rates of NNON, Pt-NNON, N-TiO_2, and Pt-N-TiO_2 samples under visible-light irradiation. During the first 2.5 h irradiation, the rate of acetone generation over Pt-NNON was as high as 8.38 ppm/min in contrast to that of NNON (0.65 ppm/min). The Pt loading photocatalyst (Pt-NNON) notably enhanced the photocatalytic performance compared with the naked photocatalyst (NNON). Namely, Pt-NNON improved over 10-fold higher activity than that of naked NNON. These results suggest that the supporting material also plays an important role in the enhancement of photocatalytic activity. In addition, the Pt-NNON exhibited a higher evolved acetone activity compared to commercial N-TiO_2 and Pt-N-TiO_2, although the

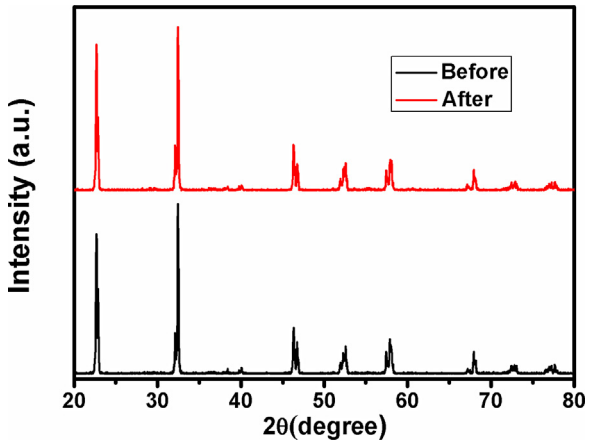

Fig. 8. X-ray diffraction patterns of Pt-NNON before and after the photocatalytic gaseous IPA degradation.

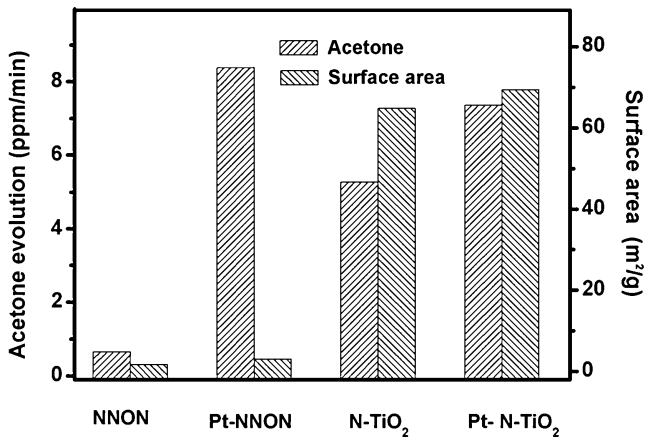

Fig. 9. Acetone evolution rates and BET surface areas of NNON, Pt-NNON, N-TiO_2, and Pt-N-TiO_2 samples.

surface area of Pt-NNON was smaller than Com N-TiO_2 (Fig. 9). The specific surface area of the present Pt-NNON photocatalyst was measured to be only ~3.0 m^2/g, which was much smaller than that of N-TiO_2 and Pt-N-TiO_2. Thus the photocatalytic activity of Pt-NNON could be enhanced by increasing the surface area (or reducing the particle size) of the catalyst. Actually, in addition to the surface areas, the electronic structures and surface structures of photocatalysts usually play a crucial role in determining their catalytic performance. Herein, we proposed the possible mechanism of the activity enhancement in Pt-NNON from the above two aspects.

As for the electric structures aspect, the calculated band structures of NNO and NNON are plotted and compared in Fig. 10. The calculated band gap of pure NNO is underestimated to be 2.48 eV (Fig. 10a) in contrast to the experimental value (3.4 eV), which is understandable since the common feature of DFT calculations in predicting band gaps due to the discontinuity in the exchange correlation potential [45]. For NNON (Fig. 10b), the position of the conduction band bottom shift little, which is similar to the observation in N-TiO_2 case that the conduction band edge remains unchanged by nitrogen-doping [46]. However, the substitutional N atoms introduce localized N 2p states above the valence band (O 2p), which should be responsible for the red shift of the absorption spectrum in the NNON (Fig. 2a).

It is acknowledged that the potential positions of conduction band (CB) and valence band (VB) of a photocatalyst are of particular importance in the process of photocatalytic decomposing organic compounds. That is, the relevant potential level of the acceptor should be more positive than (below) the conduction band potential of a photocatalyst; while the potential level of the donor is required to be more negative than (above) the valence band position of a photocatalyst. Herein, we speculated theoretically the band edge positions of NNO using the equation concerning to Mulliken electronegativity and the band gap of a semiconductor, which is described by [47,48].

$$E_{CB} = X_{NaNbO_3} - 0.5E_g \quad (1)$$

where E_{CB} and E_g are the bottom position of CB relative to vacuum energy and the band-gap energy of the semiconductor, respectively; X $\left(X = \sqrt[n]{X_1X_2X_3\ldots X_n}\right)$ means the geometric mean of the Mulliken electronegativity of the constituent atoms in the semiconductor. The Mulliken electronegativity of an atom is the arithmetic mean of the first ionization energy and the atomic electron affinity. Hence, E_{CB} was determined to be 3.73 eV relative to vacuum level, which was higher than that of $O_2/O_2^{\bullet-}$ (4.454 eV) in the view of the method inherent error (0.2 eV) [47]; while the VB edge was obtained to be 7.13 eV from the band gap. In view of the band structures calculation, the schematic diagram concerning to the band structures and the charge transfer for Pt-NNON sample is illustrated in Fig. 11. Upon visible-light irradiation, the photogenerated electrons in the CB (Nb 4d states) can be effectively transferred to the Pt nanoparticles deposited on the surface without directly recombining with holes due to the schottky barrier at the Pt and NNON interface; meanwhile, the holes remains in the VB (N 2p states) eventually forming surface reactive radicals (H_2O_2), which is responsible for the oxidative decomposition of organic pollutants.

In terms of the surface structures characteristics, as observed in FE-SEM pictures (Fig. 4), the Pt nanoparticles preferably existed at Pt-NNON nanostep areas, where are the Pt rich zones. The photoinduced electrons will migrate from the CB of NNON to Pt nanoparticles, signifying that the electrons aggregated at nanostep zones and the holes were mainly located on the other zones. On one

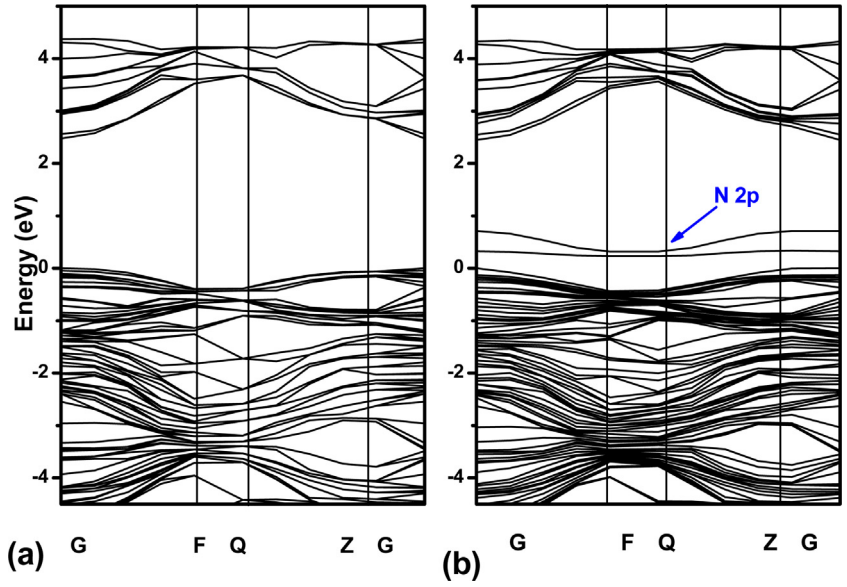

Fig. 10. The calculated band structures for (a) NNO and (b) NNON.

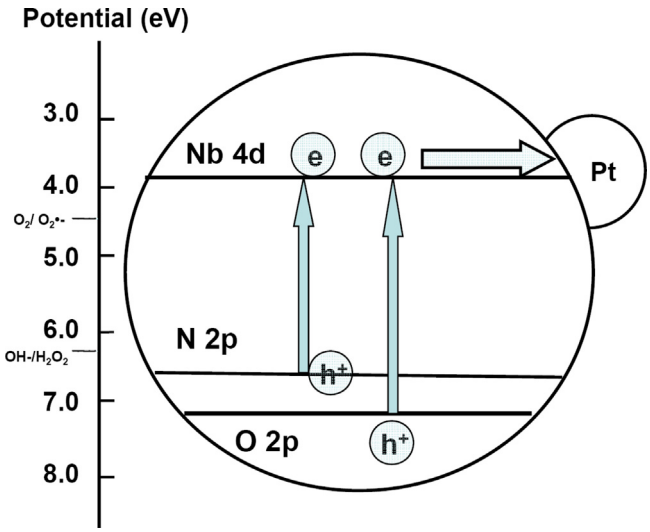

Fig. 11. Schematic diagrams of the band structures and the charge transfer for Pt-NNON sample.

hand, at the nanostep zones, electron can be efficiently reduced to $O_2^{\bullet-}$ on the highly dispersed ultrafine Pt nanoparticles. On the other hand, the other surfaces provide the catalytic active sites for holes to formation of H_2O_2. Therefore, the electrons and holes were separated through the nanostep surface structures. On the basis of above discussions, the surface nanostep structure possibly contributes to the suppression of recombination between photogenerated electrons and holes through the separation of active zones, which possibly result in the highly efficient IPA photodegradation.

4. Conclusion

In summary, Pt-NNON photocatalyst with nanostep surface microstructure was successfully fabricated by means of an in situ photodeposition method from $H_2PtCl_6{\cdot}6H_2O$ onto NNON sample, and developed as a novel visible-light-sensitive photocatalyst for organic compounds photodegradation. The FE-SEM pictures implied that Pt nanoparticles preferably existed at nanostep areas. In the photocatalytic decomposition of gaseous IPA, Pt-NNON not only exhibited 10-fold higher activity than that of NNON, but also displayed a superior performance to N-TiO_2 and Pt-N-TiO_2. The notably enhanced photocatalytic activity of Pt-NNON was attributed to the surface nanosteps and the promoted charge separation and transfer capability in Pt-NNON system. The apparent quantum efficiency of this sample for IPA photodegradation achieved up to 8.6% at the wavelength of 419 nm. This method can thus be considered as an excellent strategy to enhance photocatalytic activity of organic decomposition in addition to commonly applied noble metal doping method. Overall, the present work provides a useful insight into Pt loading photocatalysts and is likely to inform ongoing efforts to exploit materials with nanostep surface structures in the photodegradation of organic compounds.

Acknowledgements

The authors would like to acknowledge the financial support from National Natural Science Foundation of China (Nos. 21203077, 61178032, 61378037) and the Open Project Program of Key Laboratory of Eco-textiles, Ministry of Education, Jiangnan University (No. KLET1214).

Appendix A. Supplementary data

Supplementary data associated with this article can be found, in the online version, at http://dx.doi.org/10.1016/j.apcatb.2014.03.036.

References

[1] M.R. Hoffmann, S.T. Martin, W.Y. Choi, D.W. Bahnemann, Chem. Rev. 95 (1995) 69–96.
[2] A.L. Linsebigler, G.Q. Lu, J.T. Yates, Chem. Rev. 95 (1995) 735–758.
[3] R. Asahi, T. Morikawa, T. Ohwaki, K. Aoki, Y. Taga, Science 293 (2001) 269–271.
[4] H.C. Yang, S.Q. Sun, J. Zou, G. Liu, G. Smith, H. Cheng, G. Lu, Nature 453 (2008) 638–641.
[5] M. Zhang, C. Chen, W. Ma, J.C. Zhao, Angew. Chem. Int. Ed. 47 (2008) 4516–4520.
[6] R.A. Lucky, P.A. Charpentier, Adv. Mater. 20 (2008) 1755–1759.
[7] Y.B. Wang, Y.S. Wang, R. Xu, J. Phys. Chem. C 117 (2013) 783–790.
[8] H.F. Shi, Z.S. Li, J.H. Kou, J.H. Ye, Z.G. Zou, J. Phys. Chem. C 115 (2011) 145–151.
[9] H.F. Shi, T. Wang, J. Chen, C. Zhu, J.H. Ye, Z.G. Zou, Catal. Lett. 141 (2011) 525–530.
[10] W.J. Kim, D. Pradhan, B. Min, Y. Sohn, Appl. Catal. B.: Environ. 147 (2014) 711–725.
[11] J. Choi, H. Lee, Y. Choi, S. Kim, S. Lee, S. Lee, W. Choi, J.S. Lee, Appl. Catal. B: Environ. 147 (2014) 8–16.
[12] C. Lettmann, H. Hinrichs, W.F. Maier, Angew. Chem. 113 (2001) 3258–3262.
[13] S. In, A. Orlov, R. Berg, F. Garcia, S. Pedrosa-Jimenez, M.S. Tikhov, D.S. Wright, R.M. Lambert, J. Am. Chem. Soc. 129 (2007) 13790–13791.
[14] J. Wang, D.N. Tafen, J.P. Lewis, Z.L. Hong, A. Manivannan, M.J. Zhi, M. Li, N.Q. Wu, J. Am. Chem. Soc. 131 (2009) 12290–12297.
[15] S. Rodrigues, K. Ranjit, S. Uma, I.N. Martyanov, K. Klabunde, Adv. Mater. 17 (2005) 2467–2471.
[16] S. Hoang, S.W. Guo, N.T. Hahn, A.J. Bard, C.B. Mullins, Nano Lett. 12 (2012) 26–32.
[17] S. Ouyang, J.H. Ye, J. Am. Chem. Soc. 133 (2011) 7757–7763.
[18] J. Tang, Z. Zou, J. Ye, Angew. Chem. Int. Ed. 43 (2004) 4463–4466.
[19] H.F. Shi, X.L. Huang, H.M. Tian, J. Lv, Z.S. Li, J.H. Ye, Z.G. Zou, J. Phys. D: Appl. Phys. 42 (2009) 1–6.
[20] H. Kim, D. Hwang, J. Lee, J. Am. Chem. Soc. 126 (2004) 8912–8913.
[21] K. Maeda, K. Teramura, D. Lu, T. Takata, N. Saito, Y. Inoue, K. Domen, Nature 440 (2006), 295-295.
[22] X.C. Wang, X.F. Chen, A. Thomas, X.Z. Fu, M. Antonietti, Adv. Mater. 21 (2009) 1–4.
[23] J.H. Clark, M.S. Dyer, R.G. Palgrave, C.P. Ireland, J.R. Darwent, J.B. Claridge, M.J. Rosseinsky, J. Am. Chem. Soc. 133 (2011) 1016–1032.
[24] M. Murdoch, G. Waterhouse, M. Nadeem, J.B. Metson, M.A. Keane, R.F. Howe, J. Llorca, H. Idriss, Nat. Chem. 3 (2011) 489–492.
[25] J.G. Yu, L.F. Qi, M. Jaronie, J. Phys. Chem. C 114 (2010) 13118–13125.
[26] O. Rosseler, M.V. Shankar, M.K.-L. Du, L. Schmidlin, N. Keller, V. Keller, J. Catal. 269 (2010) 179–190.
[27] H. Kato, K. Asakura, A. Kudo, J. Am. Chem. Soc. 125 (2003) 3082–3089.
[28] I. Tsuji, H. Kato, H. Kobayashi, A. Kudo, J. Am. Chem. Soc. 126 (2004) 13406–13413.
[29] D.W. Jing, L.J. Guo, J. Phys. Chem. B 110 (2006) 11139–11145.
[30] J.X. Sun, G. Chen, J. Pei, R.C. Jin, Q. Wang, X.Y. Guang, J. Mater. Chem. 22 (2012) 5609–5614.
[31] A. Iwase, H. Kato, A. Kudo, Chem. Sus. Chem. 2 (2009) 873–877.
[32] G.Q. Li, S.C. Yan, Z.Q. Wang, X.Y. Wang, Z.S. Li, J.H. Ye, Z.G. Zou, Dalton Trans. (2009) 8519–8524.
[33] H.F. Shi, X.K. Li, H. Iwai, Z.G. Zou, J.H. Ye, J. Phys. Chem. Solids 70 (2009) 931–935.
[34] M.D. Segall, P.J.D. Lindan, M.J. Probert, C.J. Pickard, P.J. Hasnip, S.J. Clark, M.C. Payne, J. Phys.: Condens. Matter 14 (2002) 2717–2744.
[35] J.A. Dean, Lange's Handbook of Chemistry, 15th ed., New York, McGraw-Hill, 1999.
[36] N.C. Bigall, T. Härtling, M. Klose, P. Simon, L.M. Eng, A. Eychmüller, Nano Lett. 8 (2008) 4588–4592.
[37] Handbook of the Elements and Native Oxides, XPS International Inc., USA, 1999.
[38] J.J. Zou, C.J. Liu, K.L. Yu, D.G. Cheng, Y.P. Zhang, F. He, H.Y. Du, L. Cui, Chem. Phys. Lett. 400 (2004) 520–523.
[39] S.M. Ji, P.H. Borse, H.G. Kim, D.W. Hwang, J.S. Jang, S.W. Bae, J.S. Lee, Phys. Chem. Chem. Phys. 7 (2005) 1315–1321.
[40] Y. Maruyama, H. Irie, K. Hashimoto, J. Phys. Chem. B 110 (2006) 23274–23278.
[41] Y. Ohko, K. Hashimoto, A. Fujishima, J. Phys. Chem. A 101 (1997) 8057–8062.
[42] H.F. Shi, Z.S. Li, J.H. Ye, Z.G. Zou, J. Phys. D: Appl. Phys. 43 (085402) (2010) 1–7.
[43] J.M. Coronado, S. Kataoka, I. Tejedor, M.A. Anderson, J. Catal. 219 (2003) 219–230.
[44] F. Arsac, D. Bianchi, J.M. Chovelon, C. Ferronato, J.M. Herrmann, J. Phys. Chem. A 110 (2006) 4202–4212.
[45] A.J. Cohen, P.M. Sánchez, W. Yang, Science 321 (2008) 792–794.
[46] K.S. Yang, Y. Dai, B.B. Huang, J. Phys. Chem. C 111 (2007) 12086–12090.
[47] A.H. Nethercot, Phys. Rev. Lett. 33 (1974) 1088–1091.
[48] M.A. Butler, D.S. Ginley, J. Electrochem. Soc. 125 (1978) 228–232.